

The Point Spread Function Reconstruction by Using Moffatlets – I *

Baishun Li^{1,2}, Guoliang Li¹, Jun Cheng³, John Peterson³, Wei Cui³

¹ Purple Mountain Observatory, Chinese Academy of Sciences, Nanjing, 210000, China; *libaishun@pmo.ac.cn*

² University of Chinese Academy of Sciences, Beijing, China

³ Department of Physics, Purdue University, 525 Northwestern Ave, West Lafayette, Indiana 47907, UAS

Abstract The shear measurement is a crucial task in the current and the future weak lensing survey projects. And the reconstruction of the point spread function (PSF) is one of the essential steps. In this work, we present three different methods, including Gaussianlets, Moffatlets and EMPCA to quantify their efficiency on PSF reconstruction using four sets of simulated LSST star images. Gaussianlets and Moffatlets are two different sets of basis functions whose profiles are based on Gaussian and Moffat functions respectively. Expectation Maximization (EM) PCA is a statistical method performing iterative procedure to find principal components of an ensemble of star images. Our tests show that: 1) Moffatlets always perform better than Gaussianlets. 2) EMPCA is more compact and flexible, but the noise existing in the Principal Components (PCs) will contaminate the size and ellipticity of PSF while Moffatlets keeps them very well.

Key words: cosmology: observations - stars: imaging - techniques: image processing

1 INTRODUCTION

Gravitational lensing provides a unique way to map the matter distribution in the Universe. By measuring the shape distortion of the distant galaxies, one can gain the lensing signals and thus study the mass distribution in clusters of galaxies (Mellier 1999), large scale structures (Refregier 2003; Van Waerbeke et al. 2013; ?), and probes directly the invisible dark sector and the fundamental nature of gravity (Hoekstra & Jain 2008; Massey et al. 2010; Huterer 2010; Moffat 2006). However the shape of a galaxy can be distorted by several different mechanisms, such as 1) sheared by lensing effect. 2) convolved with a Point Spread Function (PSF). 3) pixelated on CCD and finally affected by noise. In order to recover accurately the original galaxy shape (shape right after the galaxy being lensed), decrease the statistic error and quantify the intrinsic alignments of background galaxies (Bartelmann & Schneider 2001), a number of current and planned large-area surveys were proposed, such as Euclid (Laureijs et al. 2011), LSST¹ (LSST Science

* Supported by the National Natural Science Foundation of China.

¹ <http://www.lsst.org>

Collaboration et al. 2009), WFIRST-AFTA(Spergel et al. 2015), to reduce the statistical uncertainty. On the other hand, a variety of weak lensing shear measurement algorithms (Kaiser et al. 1995; Luppino & Kaiser 1997; Hoekstra et al. 1998; Refregier & Bacon 2003) have been proposed and a series of data analysis challenges, such as GREAT08 (Bridle et al. 2010),GREAT10 (Kitching et al. 2012, 2013) and the most recent one GREAT03²³ (Mandelbaum et al. 2014), have been carried out to improve the precision and reduce systematic biases.

One of the crucial parts in reducing the systematic biases in shear measurement is modeling the point spread function (PSF) to adequate precision. The scatter and systematic bias on the size and ellipticity of the reconstructed PSF will introduce systematic bias to the shear measurement (Paulin-Henriksson et al. 2008, 2009; Massey et al. 2013). PSF is the spreading of light caused by various complex physical processes, such as diffraction by the aperture of the telescope, imperfect optics and tracking systems, temperature variations in the camera, vibrations, optical changes during telescope refocusing, and turbulence in the atmosphere (a concern for ground-based telescopes). This means that the PSF can not be represented by a simple explicit function form. Gaussian PSF was usually assumed to serve as a good approximation for most astronomical cases. But it deviates the real PSF due to the existence of wings in stellar profiles. The Moffat function is shown to describe well the presence of wings (when the value of β is taken properly) and contain the Gaussian function as a limiting case (when $\beta \rightarrow \infty$) (Trujillo et al. 2001). However to reproduce PSF arriving the weak lensing precision, high-order correction is required. Based on a technique called Shapelets (Refregier 2003; Refregier & Bacon 2003; Massey & Refregier 2005), which decompose an object using a series of localised basis functions and compress the information of shape in a small number of expansion coefficients. In this paper, we use the Gaussian and Moffat function as primary profiles to create two basis function sets which we call Gaussianlets and Moffatlets (Li et al. 2013) respectively to decompose the PSF.

The minimum number of 50 stars over which the PSF must be calibrated in order to control the systematic errors to a level similar to the statistical errors has been estimated for the future ambitious surveys (Paulin-Henriksson et al. 2008). With this ensemble of stars in an image, a set of Principal Components (PCs) can be solved via performing the statistical procedure called principal component analysis (PCA) . In Bailey 2012, a framework called Expectation Maximization (EM) PCA is introduced that extended the classical PCA to a form that can incorporate estimates of measurement variance while solving for the PCs. In this paper we use this method to find the PCs of PSF.

This article is organized as follows. In section 2 we describe the three methods, Gaussianlets, Moffatlets and EMPCA, and their algorithms for reconstructing PSFs. In section 3 we describe the simulate structure of the data we use. And in section 4 we perform the numerical tests of our three methods and compare their reconstruction efficiency. Finally we conclude by discussing the limitations and prospects of our algorithm in section 5.

² <http://great3challenge.info>

³ <http://great3.projects.phys.ucl.ac.uk/leaderboard/>

2 RECONSTRUCTION METHODS

2.1 Gaussianlets and Moffatlets

The so-called Gaussianlets here, is a reduced version of shapelets ([Massey & Refregier 2005](#)) where we only keep the basis functions with $m = 0$. The explicit mathematical formula of Gaussianlets is

$$P_l(r) = \frac{1}{\sqrt{\pi\sigma_d^2}} e^{-\frac{r^2}{2\sigma_d^2}} L_l\left(\frac{r^2}{\sigma_d^2}\right), \quad (1)$$

The basis functions in Moffatlets are also circular symmetric and contain no angular components. The formula (see [Appendix A](#) for more details) is

$$Q_l(r) = \sqrt{\frac{2\beta-1}{\pi r_d^2}} L_l[v(r)] \left[1 + \left(\frac{r}{r_d}\right)^2\right]^{-\beta}, \quad (2)$$

where

$$v(r) = \left(\frac{1}{2\beta} - 1\right) \ln\left[1 + \left(\frac{r}{r_d}\right)^2\right]^{-2\beta} \quad (3)$$

In both (1) and (2), $L_l(x)$ is the Laguerre polynomials:

$$L_l(x) = \frac{e^x}{l!} \frac{d^l}{dx^l} (e^{-x} x^l) = \frac{1}{l!} \left(\frac{d}{dx} - 1\right)^l x^l. \quad (4)$$

where l runs from 0 to ∞ . Mathematically both sets of basis functions are orthogonalized and normalized in the following sense,

$$\int_0^{+\infty} P_l(r) P_m(r) dr = \int_0^{+\infty} Q_l(r) Q_m(r) dr = \delta_{lm}. \quad (5)$$

There are free parameters (σ_d in Gaussianlets and (β, r_d) in Moffatlets) that are adjustable in the basis functions. Tuning their values we can change the size and steepness of the basis functions' radial variation. In the process of modeling, these free parameters are adjusted to the values that best fit to the data, which means the shape of the 0th order function is mostly close to the averaged shape of a set of stellar profiles. In this case, the expansion is made sure to be very compact.

Using these basis functions, we can reproduce the star images as follows:

- 1) Calculate the center and ellipticity for each stellar profile using the fast fitting algorithms [Li et al. 2012](#).
- 2) According to the center and ellipticity of each star, the shape parameters of Gaussian and Moffat model are also calculated using the fast fitting algorithm (see [Li et al. 2012](#)). [Trujillo et al. 2001](#) argued that a Moffat function could be used to reliably model the turbulence prediction when $\beta \sim 4.765$. However, the PSFs usually measured in real images have bigger wings, or equivalently smaller values of β ($2.5 < \beta < 4$; see [Saglia et al. 1993](#)), than those expected from the turbulence theory. In this paper, we simply set $\beta = 3.5$.

(3) Calculate the mean of the best-fitting parameters over all stars. And use the mean as the value of parameter(s) in the basis functions to create a set of basis functions we will use then.

(4) Finally for each star image, we squeeze the circular symmetric basis functions to the same ellipticity as the star has by performing coordinate transformation and then decompose the star image into several elliptical basis functions. The basis functions have to be pixelated on a finite region in order to perform numerical simulation. This causes

violation of the orthogonality and the coefficients of each basis function can not be simply derived from inner product. We overcome this difficulty by solving a Maximum-likelihood solution(e.g., [Andrae et al. 2011](#)).

Finally we have two parameters (e_1, e_2) and several coefficients of basis functions for each star. The first eight basis functions of Gaussianlets (first row) and Moffatlets (second row) are shown in Fig. 1. We can see that Moffatlets are more extended than Gaussianlets. This property will lead Moffatlets method to show good performance in the reconstruction of star image.

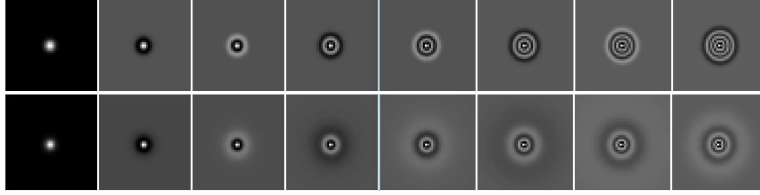


Fig. 1 A demonstration of the first eight basis functions of Gaussianlets (first row) and Moffatlets (second row) constructed in the program respectively. From left to right, as the order of the basis functions increases, the number of circles increase. As you will also notice, Moffatlets basis functions are "fatter" than Gaussianlets basis functions.

2.2 EMPCA

The EMPCA method is an extended version of the classical PCA. It uses expectation and maximization steps to subtract the eigenvectors. The most important improvement is that the noise in the data can also be taken into account ([Bailey 2012](#)). These improvements provide a high-efficiency calculation and reasonable handling of noise. We adopts per-variable weight strategy in this work which can be summarized as follows. The χ^2 -fucntion is defined as

$$\chi^2 = \sum_{vari, obsj} w_{ij} (A_{ij} - \phi_i c_j)^2, \quad (6)$$

For given eigenvector ϕ , the E-step gives the optimal coefficient as:

$$c_j \leftarrow \frac{\sum_i w_{ij} A_{ij}}{\sum_i w_{ij} \phi_i^2}, \quad (7)$$

Then the M-step improves the eigenvector as:

$$\phi_i \leftarrow \frac{\sum_j w_{ij} c_j A_{ij}}{\sum_j w_{ij} c_j^2}. \quad (8)$$

where $A_{ij} = (a_1, \dots, a_{N_{star}})$ is initially the dataset in which a_j is a vector denoting the j th star, ϕ_i is initially the 1st PC we are searching for and c_j is the decomposition coefficient of the j th star on the PC. The goal is to solve the minimization problem of (6) incorporating a weights matrix w_{ij} . The algorithm starts with an arbitrary ϕ , and then updates ϕ through E-step and M-step iteratively until converged. To find the higher-order PCs, we replace A by $(A - \phi c)$ and repeat the above process. This procedure can be continued until there are no more effective PCs show up.

The weight is simply related to the noise in each pixels as $w_{ij} = 1/\sigma_{ij}^2$. Our simulated stars contain Poisson and Gaussian noise. The estimation of σ_{ij} is given by the following rule: a Gaussian noise σ is evaluated on the outskirts of each star stamps, then for pixel with value I smaller than 2σ , we take $\sigma_{ij} = \sigma$, for pixel value I larger than 2σ , we take $\sigma_{ij} = \sqrt{\sigma^2 + gI}$, where g is the gain of CCD.

3 DATA DESCRIPTION

In this paper, we invoke PhoSim (Peterson et al. 2015), our primary tool for generating simulated images. PhoSim uses a photon Monte Carlo approach to construct images by sampling photons from models of astronomical source populations. PhoSim is designed to represent Large Synoptic Survey Telescope (LSST) performance and generates images expected for LSST with high fidelity. All detailed atmosphere, telescope and camera physical effects that determine the shapes, locations and brightnesses of individual stars and galaxies can be accurately represented. This makes PhoSim a perfect simulation tool for study of PSF.

To examine the PSF effects four images are generated using PhoSim version 3.4. We simulate images for two LSST chips: R22_S11 indicates center chip in the focal plane while R02_R01 indicates a chip near the edge of the focal plane. In PhoSim all the physical effects can be separately turned 'on' and 'off' so that we can have control over the effects which may affect PSF. Two of the images are simulated with diffraction 'off' and the other two with diffraction 'on'. For all the other physical effects default settings of LSST are used.

In the four images, the pixel size is $0.2''/\text{pixel}$ and the pixel values are simulated in ADU unit with gain=1, hence the value on each pixel counts the number of photons fall in. The star images contains only Poisson noise and all have roughly the same magnitude. We can then add different amounts of background Gaussian noise to each star and estimate the signal-to-noise ratio (SNR) within a 10×10 square around the brightest pixel by using definition $\text{SNR} = \Sigma_p(I_p) / \sqrt{\Sigma_p(\sigma^2 + I_p)}$, where I_p is the LSST simulator data with only Poisson noise, σ is the Gaussian noise we added in later.

Based on our simulation, an explicit model fitting is also performed as a verification of the result in Trujillo et al. 2001, they claimed that the Moffat function is the better model for fitting PSFs than Gaussian function. We choose several bright stars from our simulation and then fit them with these two models respectively by minimizing the χ^2 function:

$$\chi^2 = \sum_{i,j} \frac{(I_{ij}^0 - F_{ij})^2}{\sigma_{ij}^2}, \quad (9)$$

where F_{ij} is the fitting function and σ_{ij} is the Poisson noise in each pixel.

Fig.2 shows the fitted brightness profile along the diagonal for our four kinds of simulated stars. Clearly, Moffat model can fit our simulated stars much better than Gaussian profile. The Gaussian profile only fits the inner part well but drops too fast in the outer region. Meanwhile the fitting of the Moffat model is well behaved even at large radius. Therefore we would expect that Moffatlets will also work better than Gaussianlets in the following tests.

One hundred stars are randomly selected from each CCD. The test is then divided into four cases: In the first three cases, an uniform level of Gaussian noise is added to the 100 stars with $\sigma = 10, 40, 80$ (with $\langle \text{SNR} \rangle \approx 416, 232$ and 132) respectively; in the fourth case, different amounts of Gaussian noise with the value of σ randomly ranging from 10

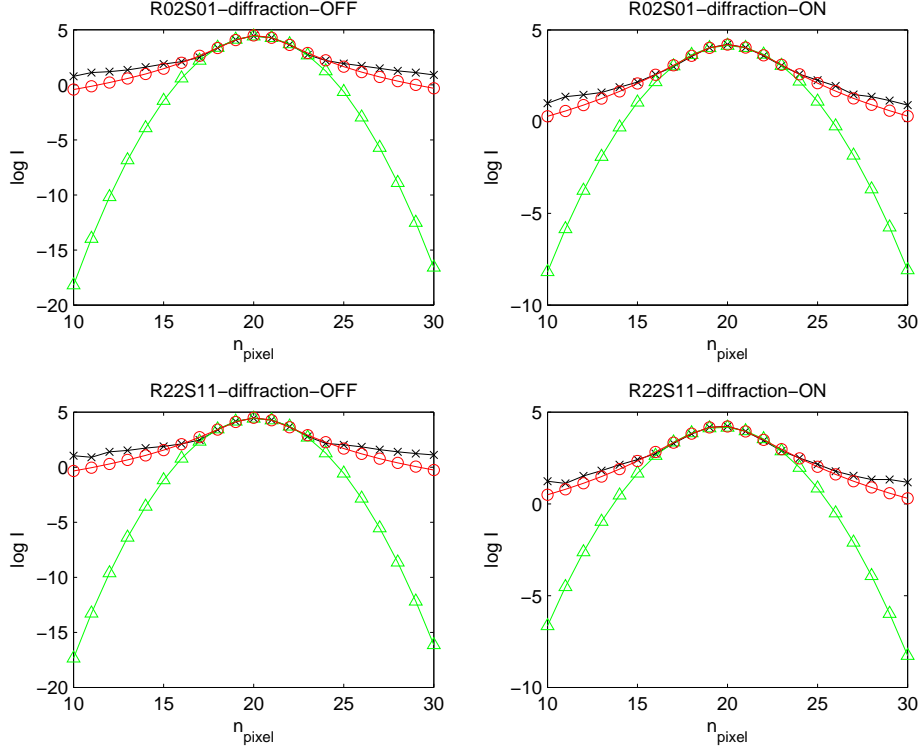


Fig. 2 After computing the best fits for parameters σ and r_d , we construct the corresponding Gaussian (green dots and lines) and Moffat (red dots and lines) functions and compare to the original star profiles (black dots and lines). The drawn curves are only the cross-sections of the 2-dim images.

to 100 are added to the stars. By including the last case, we try to mimic 100 stars of different SNR ($80 \lesssim \text{SNR} \lesssim 500$), or in terms of observations, there are 100 stars with different magnitudes. Fig. 3 shows these four cases of R02S01-diffraction-OFF simulation.

4 RESULTS

The reconstructions using the three methods are performed on the noise interfered data in all four cases. we aim to test how efficient are these three methods and how the noise affect the results. For the basis function methods, the shape parameters are computed according to the average shapes of the 100 stars. The value of σ_d and r_d in the Gaussianlets and Moffatlets are listed in Table. 1 and Table. 2 respectively. It shows that value of σ_d and r_d taken for "diffraction on" data are larger than "diffraction off" data. This is because spikes exist in "diffraction on" data and make the stars more extended. Once the parameters are fitted, we can create the basis functions. Fig. 1 demonstrates the first 8 basis functions of Gaussianlets and Moffatlets respectively.

Noise affects the EMPCA method in a very apparent way. In Fig. 4, a set of patterns were clearly resolved by the PCA algorithm in case 1($\sigma = 10$). But as more noise is added, less useful PCs will be extracted. Just as shown in case 2($\sigma = 40$), case 3($\sigma = 80$) and case 4($\sigma = \text{ran}(10 - 100)$), all the high-order PCs contain visible noise and no signal

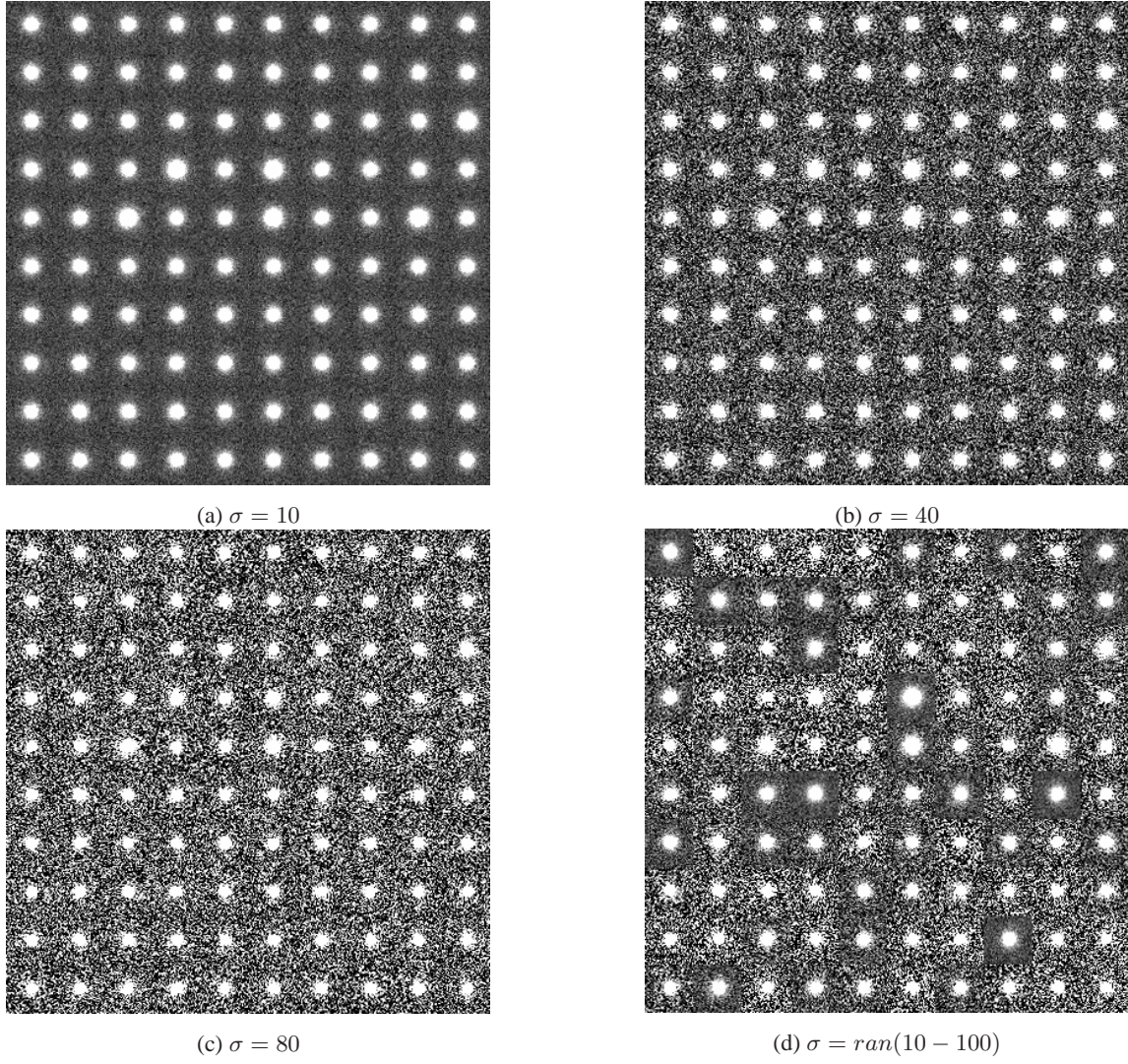


Fig. 3 The four panels show background noise added in four different cases. All pictures are drawn in the same gray scale.

can even be easily recognized in some of them. This introduces uncertainty to appropriately choose the number of the PCs to be used in the EMPCA method.

	10	40	80	ran(10-100)
R02S01-diffraction-OFF	1.419150	1.419232	1.419417	1.419747
R02S01-diffraction-ON	1.906670	1.904350	1.904945	1.906408
R22S11-diffraction-OFF	1.443192	1.442398	1.442060	1.440537
R22S11-diffraction-ON	1.921579	1.919953	1.920336	1.921725

Table 1 Value of σ_d taken in different simulation runs

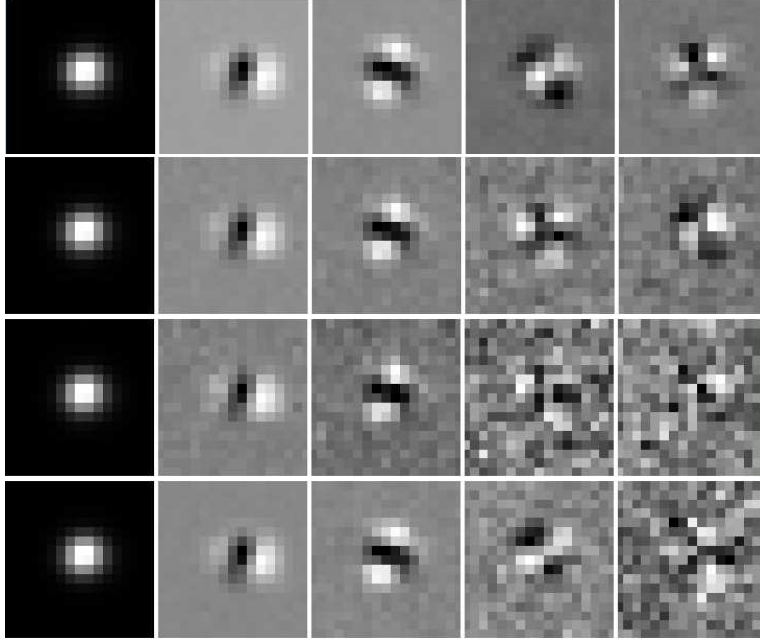


Fig. 4 The first five PCs extracted in different cases. The first row is the case that we add to the data Gauss noise of $\sigma = 10$. In this case we can see the most amount of signals. The other three rows are cases of $\sigma = 40, 80$ and $\text{ran}(10 - 100)$ respectively. As the noise increased, less and less signal can be recognized in the higher order PCs.

Here we introduce the usual χ^2 function to quantify how well the reconstruction is done.

$$\chi^2 = \sum_{i,j} \frac{(I_{ij}^0 - I_{ij}^{(reconstructed)})^2 w_{ij}}{N_{pixels}}, \quad (10)$$

I^0 refers to the original extracted star with poisson noise only. The weight is the same as we employed in the EMPCA algorithm.

We draw the χ^2 -curves corresponding to reconstructions using different number of PCs (Fig. 5) (The reconstruction is performed on image R02S01-diffraction-OFF, $\sigma = 40$). The green line which corresponds to using 3 PCs is the lowest one. As we decrease the number of used PCs, the χ^2 -curve raises up (as the black line of 1 PC indicates) since fewer PCs means less information is taken into account. As we increase the number of used PCs, the χ^2 -curve also raises up due to the fact that more noise are contained in the reconstructed star images. In fact, we can see that using 7 PCs is worse than using just 1 PC. In the following reconstructions, applied to all data sets, we always use 4 PCs.

	10	40	80	ran(10-100)
R02S01-diffraction-OFF	3.030692	3.029967	3.029196	3.029439
R02S01-diffraction-ON	4.061016	4.052640	4.051725	4.054829
R22S11-diffraction-OFF	3.083501	3.080003	3.077113	3.072700
R22S11-diffraction-ON	4.094765	4.089887	4.085220	4.086687

Table 2 Value of r_d taken in different simulation runs

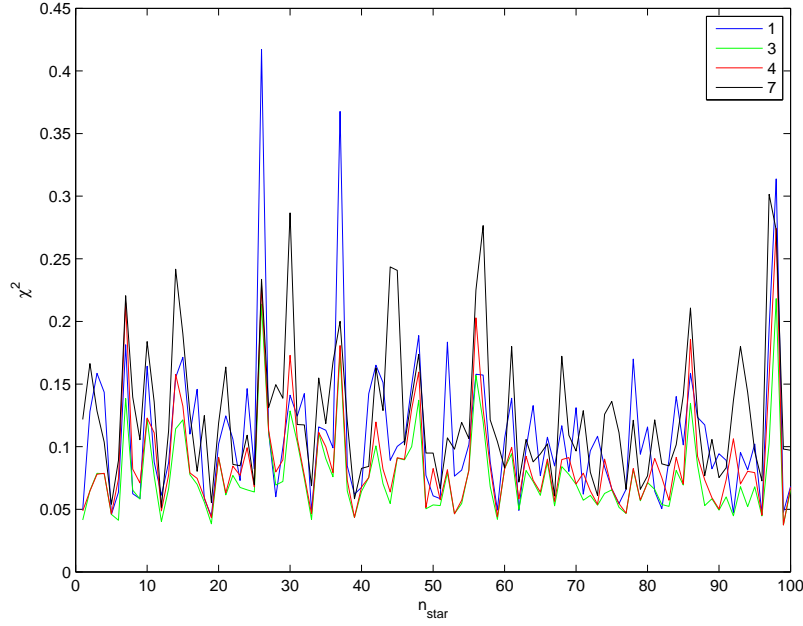


Fig. 5 The χ^2 of reconstructions by using different number of PCs are compared. n_{star} is the id of the star. The blue line correspond to reconstructions done by only 1 PC. The green, red and black lines are that of 3,4 and 7 PCs used correspondingly. The green line is the lowest one indicating the best fit.

As for our basis function methods, we would expect more number of free parameters because the theoretical basis functions can not be more compact than the numerically solved PCs. Since there are already two parameters(e_1, e_1) for each star, we simply adopt four basis functions for Moffatlets and Gaussianlets method.

Using the χ^2 quantity, the three methods are compared for all data sets in Fig. 6, 7, 8, 9, where the blue, red and green lines are for the results of EMPCA, Moffatlets and Gaussianlets respectively. All of these results broadly support the same conclusions: 1) EMPCA always performs better than Moffatlets and Gaussianlets for the high SNR cases. This is because there are high-order patterns of brightness distribution in star images which can not be described by our elliptical basis functions but can be resolved by EMPCA. But for the low SNR cases, the results of EMPCA are comparable with the results of Moffatlets. 2) Moffatlets is always better than Gaussianlets. As mentioned in the introduction and also in [Trujillo et al. 2001](#), that Moffat function fit real PSF better than Gaussian function. Gaussianlets performs especially poorly in case 1 since the Gaussian function cannot describe the presence of large "wings" in PSF which is not buried by noise in this case. The several high peaks indicated by green line in case 4($\sigma = \text{ran}(10 - 100)$) correspond the stars with higher SNRs. We also see the "diffraction on" stars can be reconstructed better than "diffraction off" stars. This is because in our simulation the diffraction spikes are not very sharp rather it makes the stars more extended and smooth some high order minor substructures.

Another two quantities are also introduced to serve as test for the efficiency of the reconstructions. The first quantity is the ellipticity defined as:

$$e_1 = \frac{Q_{11} - Q_{22}}{Q_{11} + Q_{22}}, \quad (11)$$

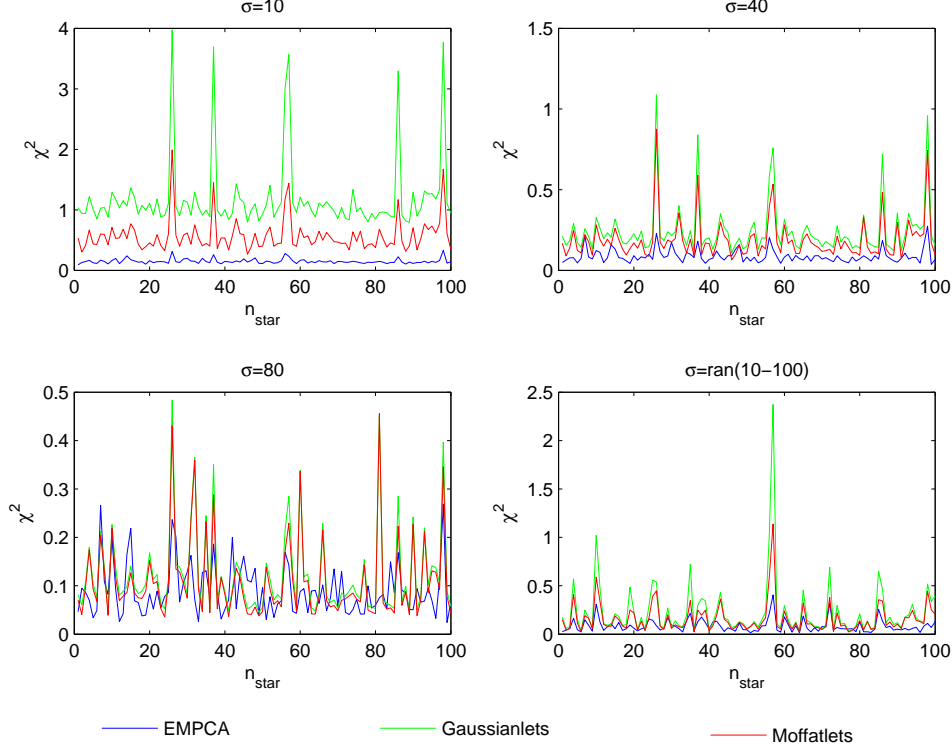


Fig. 6 χ^2 -curves in the test of data set R02S01-diffraction-OFF. Blue lines are for EMPCA, green lines for Gaussianlets and red lines for Moffatlets. The same denotement is adopted in the next χ^2 -plots Fig. 7, 8, 9 and δR^2 -plots Fig. 10, 11, 12, 13.

$$e_2 = \frac{2Q_{12}}{Q_{11} + Q_{22}}. \quad (12)$$

where Q_{ij} are second brightness moments of star image. A Gaussian filter is employed in calculating the moments. The FWHM of the Gaussian filter is the mean FWHM of stars.

The other quantity is the square rms size of star defined as,

$$R^2 = Q_{11}^2 + Q_{22}^2 \quad (13)$$

Using these formulas, we first measure (R^2, e_1, e_2) for the original stars without Gaussian noise added yet. Then we calculate (R^2, e_1, e_2) for the reconstructed stars in each realizations. Finally we compare the differences between the two, $(\delta R^2, \delta e_1, \delta e_2)$. Fig. 10, 11, 12, 13 compare δR^2 . As above, the blue, red and green lines are for the results of EMPCA, Moffatlets and Gaussianlets respectively. It shows Moffatlets fit the size of stars best (the average δR^2 over 100 stars is close to 0 and the scatter is very small) and Gaussianlets did worst (the average δR^2 always biases from 0 a lot although its scatter is also small. As shown in Fig. 2, Gaussian function descends too fast at large radius, hence Gaussianlets underestimate the sizes of PSFs with presence of large "wings"). EMPCA also does well but introduces larger scatters because of the noise in the PCs.

Fig. 14, 15, 16, 17 compare the uncertainty in ellipticity. The black dots show the ellipticity (e_1, e_2) measured from original stars (without background noise added yet) and the colored dots show the deviations of ellipticity $(\delta e_1, \delta e_2)$

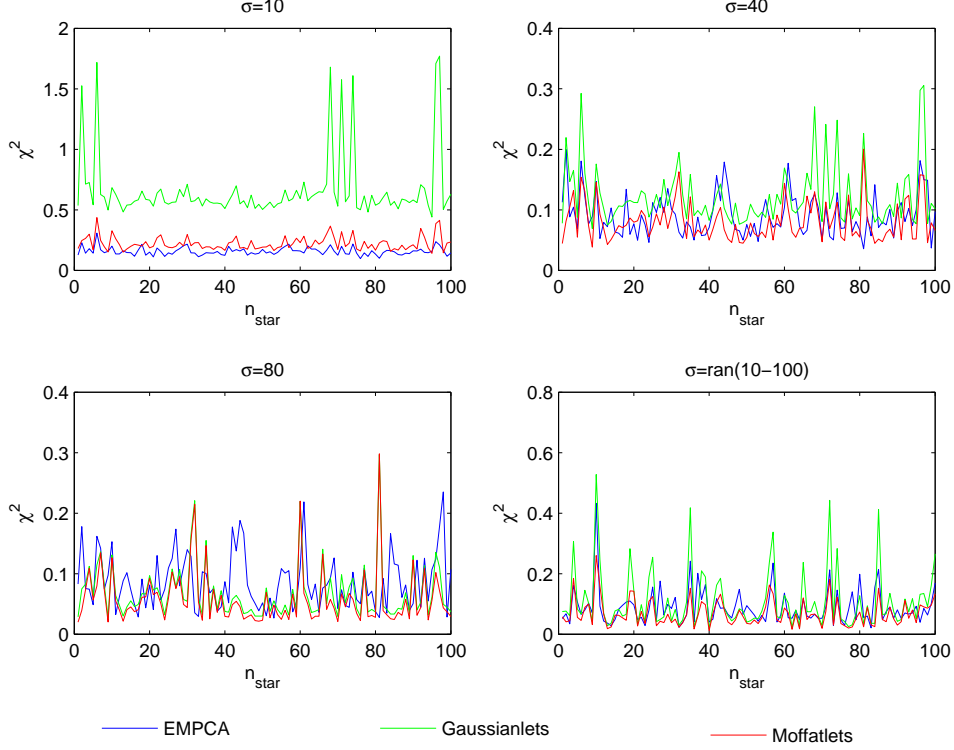


Fig. 7 χ^2 -curves in the test of data set R02S01-diffraction-ON.

between reconstructed stars and original stars. For the basis function methods, the ellipticity are measured first for all stars and the basis functions are then correspondingly reshaped. Therefore the Moffatlets and Gaussianlets method share the same ellipticity and we just plot the results of Moffatlets here. The ellipticity are measured from the Gaussian noise added data, so when the noise increases, the scatter in ellipticity increase.

As we can see that the basis function methods fit the ellipticity of stars much better than EMPCA. Although EMPCA performs well on the χ^2 test, but introduced larger scatters in the size, especially in the ellipticity of PSF. This implies more stars are needed in EMPCA method in order to reconstruct an unknown PSF's size and ellipticity to required accuracy. We calculate σ_{R^2}/R^2 and σ_e in different simulation runs, the results are listed in Table.3,4,5 and Table.6,7. As shown in [Paulin-Henriksson et al. 2008](#), uncertainties on size and ellipticity of PSF calibration is the two key parameters which will propagate into the systematics of shear measurement. The requirement for systematic bias of the cosmic shear measurement, $\sigma_{sys}^2 \lesssim 10^{-7}$ would ask $\sigma_{R^2}/R^2 \lesssim 10^{-3}$ and $\sigma_e \lesssim 10^{-3}$. This requirement will be a big challenges for the PSF reconstruction methods using PCA. Moffatlets fit the requirement very well but just because no sharp spikes presented in the data. It's an issue to model sharp spikes using circular symmetric Moffatlets.

5 CONCLUSIONS AND DISCUSSION

We use three methods to reconstruct the simulated star images. The basis function methods use smooth functions which have explicit formulas and easily to be created. As our test results have shown, Moffatlets performed better in

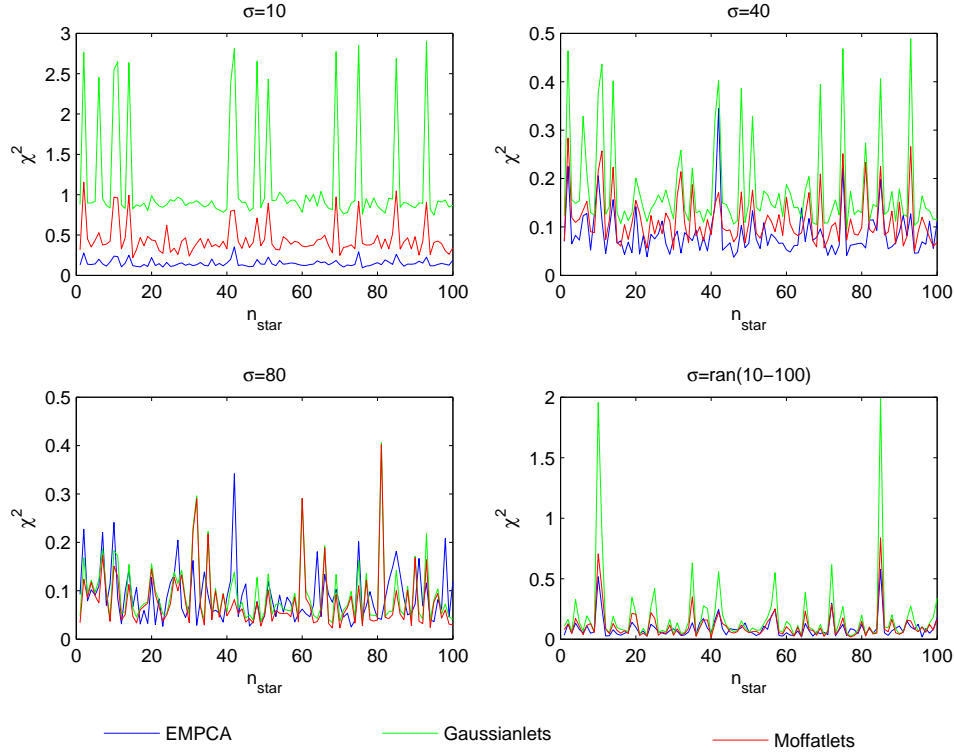


Fig. 8 χ^2 -curves in the test of data set R22S11-diffraction-OFF.

image reconstructions than Gaussianlets. This is mainly because the Moffat function is a better PSF model than the Gaussian function.

Due to the pixelization and finite size, our basis functions are not exactly orthogonal to each other. This will rise cross-correlation between the coefficients. Numerical orthogonolization algorithms, such as Gram-Schmidt process or

	10	40	80	ran(10-100)
R02S01-diffraction-OFF	0.0080	0.0148	0.0280	0.0209
R02S01-diffraction-ON	0.0079	0.0136	0.0223	0.0150
R22S11-diffraction-OFF	0.0066	0.0128	0.0234	0.0198
R22S11-diffraction-ON	0.0074	0.0108	0.0201	0.0163

Table 3 Value of $[\sigma_{R^2}/R^2]$ for EMPCA in different simulation runs.

	10	40	80	ran(10-100)
R02S01-diffraction-OFF	0.0058	0.0090	0.0160	0.0149
R02S01-diffraction-ON	0.0026	0.0055	0.0101	0.0081
R22S11-diffraction-OFF	0.0072	0.0093	0.0147	0.0151
R22S11-diffraction-ON	0.0024	0.0048	0.0087	0.0075

Table 4 Value of $[\sigma_{R^2}/R^2]$ for Moffatlets in different simulation runs.

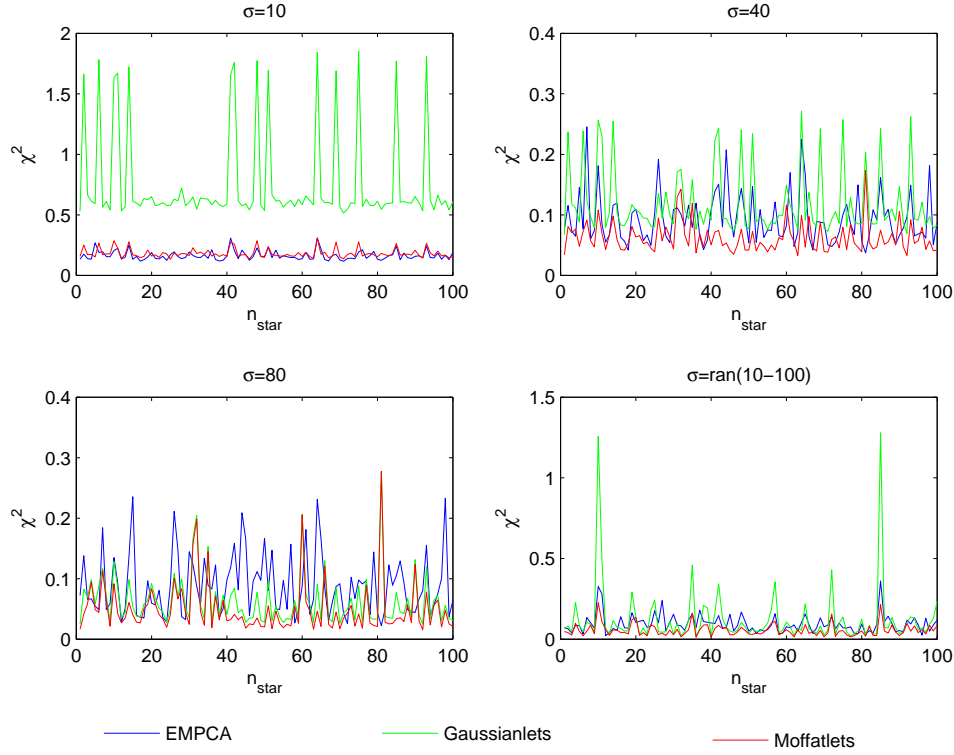


Fig. 9 χ^2 -curves in the test of data set R22S11-diffraction-ON.

Householder transformation can be applied to resolve this problem. The basis function methods use circular symmetric functions which are then shaped into elliptical ones according to the premeasured ellipticity of stars. As a result, they only consider the radial variation. High-order angular structures, such as diffraction spikes, usually appear in the realistic PSFs and will introduce bias into our results in principle. Our tests show that this is not a big issue in our

	10	40	80	ran(10-100)
R02S01-diffraction-OFF	0.0635	0.0636	0.0647	0.0672
R02S01-diffraction-ON	0.0103	0.0111	0.0134	0.0142
R22S11-diffraction-OFF	0.0578	0.0576	0.0581	0.0611
R22S11-diffraction-ON	0.0100	0.0106	0.0123	0.0130

Table 5 Value of $[\sigma_{R^2}/R^2]$ for Gaussianlets in different simulation runs.

	10	40	80	ran(10-100)
R02S01-diffraction-OFF	0.0018	0.0029	0.0037	0.0028
R02S01-diffraction-ON	0.0018	0.0025	0.0037	0.0035
R22S11-diffraction-OFF	0.0013	0.0017	0.0030	0.0031
R22S11-diffraction-ON	0.0016	0.0027	0.0043	0.0040

Table 6 Value of σ_e for EMPCA method in different simulation runs.

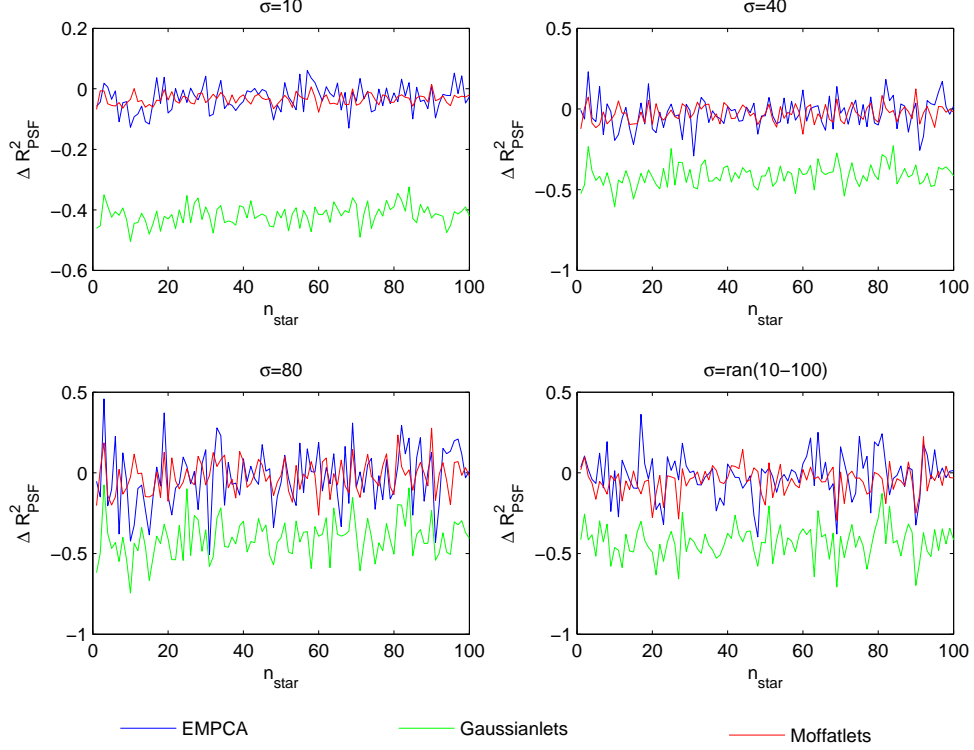


Fig. 10 δR^2 -curves in the test of data set R02S01-diffraction-OFF.

simulated LSST images since the presented diffraction spikes are not very sharp and Moffatlets can reconstruct very well at least in terms of ellipticity and size of PSF. The more detailed studies on the issue of sharp diffraction spikes is beyond the scope of this paper.

The EMPCA method has several advantages than the basis function method: 1)The resolved PCs are compact and flexible. It's the most efficient way to reconstruct the irregular images. 2)The PCs are orthogonal to each other, this makes their coefficients independent and can be interpolated easily. While PCA method also has defects, the resolved PCs contain noise inevitably. This would introduce relatively higher scatter in the size and ellipticity in the reconstructed PSF and then rise higher systematic bias in the cosmic shear measurement.

The current PSF reconstructions is still not accurate enough to produce satisfying shear measurement for weak lensing surveys. The high-order angular structures like diffraction spikes has not been considered in detail in this paper. Meanwhile our tests have shown that the Moffatelets is a very promising tool for the PSF reconstruction. In the

	10	40	80	ran(10-100)
R02S01-diffraction-OFF	0.0009	0.0010	0.0013	0.0012
R02S01-diffraction-ON	0.0004	0.0004	0.0005	0.0005
R22S11-diffraction-OFF	0.0006	0.0007	0.0009	0.0009
R22S11-diffraction-ON	0.0004	0.0004	0.0005	0.0005

Table 7 Value of σ_e for Moffatlets/Gaussianlets in different simulation runs.

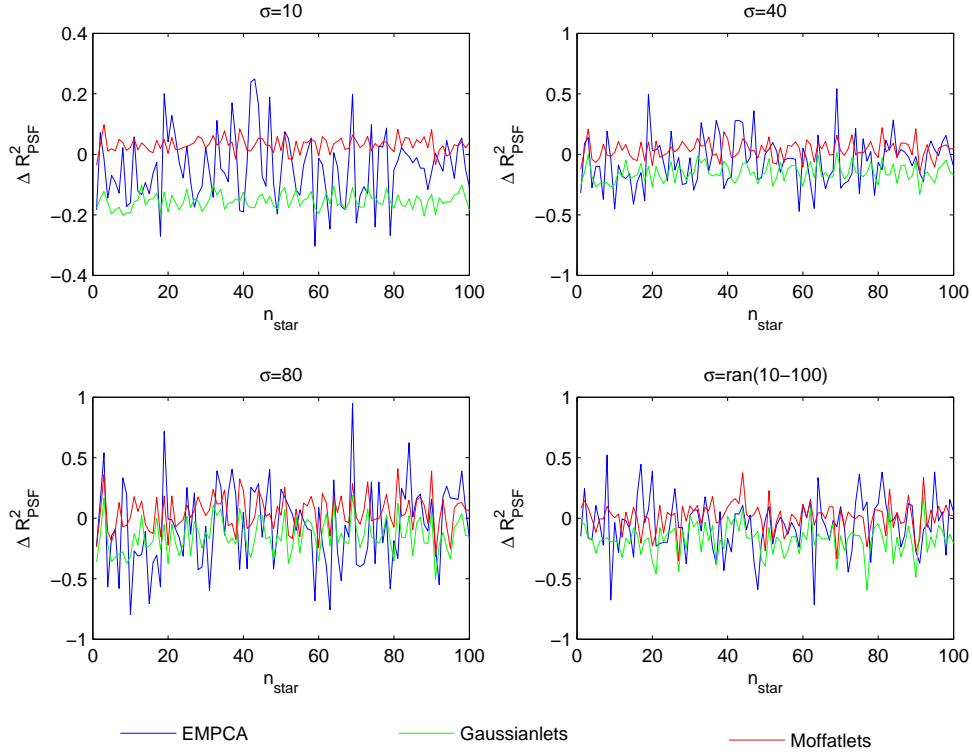


Fig. 11 δR^2 -curves in the test of data set R02S01-diffraction-ON.

future studies, we will combine the angular structures of Moffatlets and EMPCA techniques together to search PCs in a finite Moffatlets space.

ACKNOWLEDGEMENTS

BS and GL are supported by the National Key Basic Research Program of China (2015CB857000), the Strategic Priority Research Program the Emergence of Cosmological Structures of the Chinese Academy of Sciences (XDB09000000). GL also thanks the supports from the One-Hundred-Talent fellowships of CAS and the NSFC grants (11273061 and 11333008). BS acknowledge the support from the NSFC grant (11403103). JC, JRP and WC acknowledge the supports from Purdue University, the Department of Energy (DE-SC00099223), and the LSST Project (C44054L).

References

- Bartelmann, M., & Schneider, P. 2001, 340, 291
- Alcock, C., Allsman, R. A., Alves, D. R., et al. 2000, 542, 281
- Cooray, A., & Sheth, R. 2002, 372, 1
- Mellier, Y. 1999, 37, 127
- Refregier, A. 2003, 41, 645
- Van Waerbeke, L., Benjamin, J., Erben, T., et al. 2013, 433, 3373

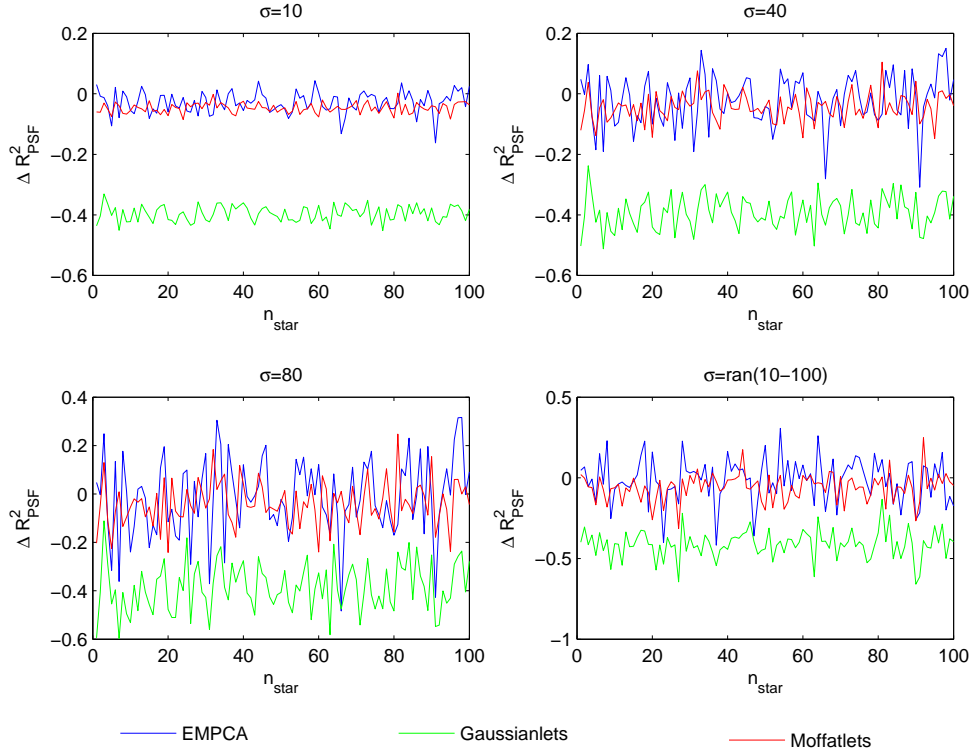


Fig. 12 δR^2 -curves in the test of data set R22S11-diffraction-OFF.

Planck Collaboration, Ade, P. A. R., Aghanim, N., et al. 2015, arXiv:1502.01589

Persic, M., Salucci, P., & Stel, F. 1996, 281, 27

Riess, A. G., Strolger, L.-G., Tonry, J., et al. 2004, 607, 665

Moffat, J. W. 2006, arXiv:astro-ph/0608675

Hoekstra, H., & Jain, B. 2008, Annual Review of Nuclear and Particle Science, 58, 99

Massey, R., Kitching, T., & Richard, J. 2010, Reports on Progress in Physics, 73, 086901

Huterer, D. 2010, General Relativity and Gravitation, 42, 2177

Laureijs, R., Amiaux, J., Arduini, S., et al. 2011, arXiv:1110.3193

LSST Science Collaboration, Abell, P. A., Allison, J., et al. 2009, arXiv:0912.0201

Spergel, D., Gehrels, N., Baltay, C., et al. 2015, arXiv:1503.03757

Kaiser, N., Squires, G., & Broadhurst, T. 1995, 449, 460

Luppino, G. A., & Kaiser, N. 1997, 475, 20

Hoekstra, H., Franx, M., Kuijken, K., & Squires, G. 1998, 504, 636

Refregier, A., & Bacon, D. 2003, 338, 48

Bridle, S., Balan, S. T., Bethge, M., et al. 2010, 405, 2044

Kitching, T. D., Balan, S. T., Bridle, S., et al. 2012, 423, 3163

Kitching, T. D., Rowe, B., Gill, M., et al. 2013, 205, 12

Mandelbaum, R., Rowe, B., Bosch, J., et al. 2014, 212, 5

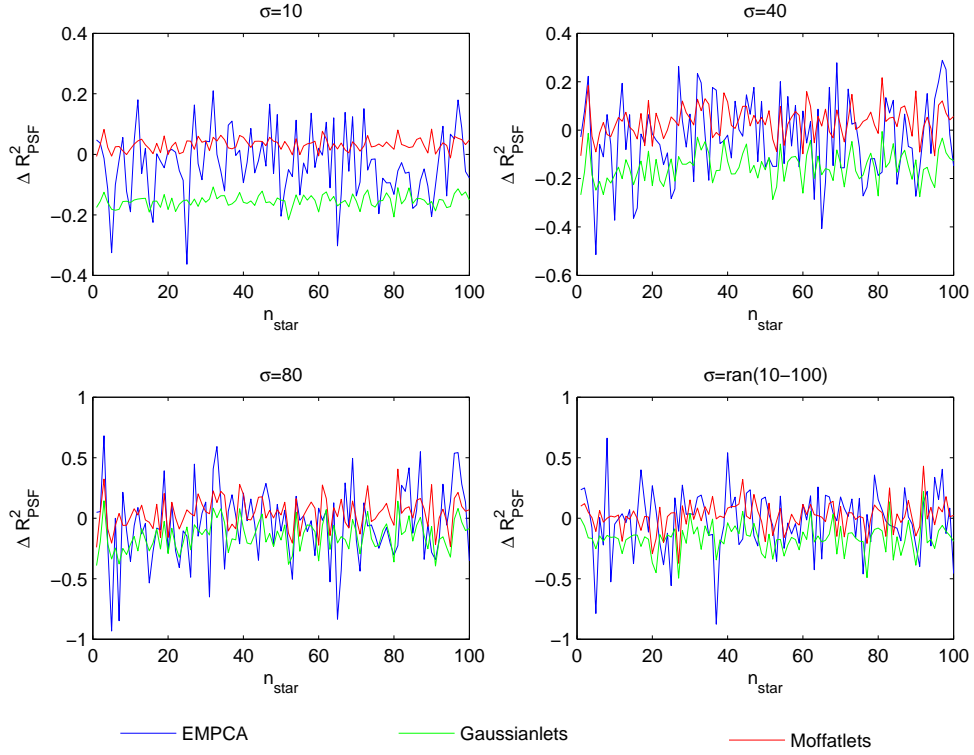


Fig. 13 δR^2 -curves in the test of data set R22S11-diffraction-ON.

Paulin-Henriksson, S., Amara, A., Voigt, L., Refregier, A., & Bridle, S. L. 2008, 484, 67

Paulin-Henriksson, S., Refregier, A., & Amara, A. 2009, 500, 647

Massey, R., Hoekstra, H., Kitching, T., et al. 2013, 429, 661

Bergé, J., Price, S., Amara, A., & Rhodes, J. 2012, 419, 2356

Massey, R., & Refregier, A. 2005, 363, 197

Refregier, A. 2003, 338, 35

Li, G., Xin, B., & Cui, W. 2013, *Astrophysics from Antarctica*, 288, 306

Bailey, S. 2012, 124, 1015

Saglia, R. P., Bertschinger, E., Baggle, G., et al. 1993, 264, 961

Andrae, R., Melchior, P., & Jahnke, K. 2011, 417, 2465

Li, G., Xin, B., & Cui, W. 2012, arXiv:1203.0571

Shlens, J. 2014, arXiv:1404.1100

Kitching, T., Balan, S., Bernstein, G., et al. 2010, arXiv:1009.0779

Trujillo, I., Aguerri, J. A. L., Cepa, J., & Gutiérrez, C. M. 2001, 328, 977

Hu, W. 1999, 522, L21

Peterson, J. R., Jernigan, J. G., Kahn, S. M., et al. 2015, 218, 14

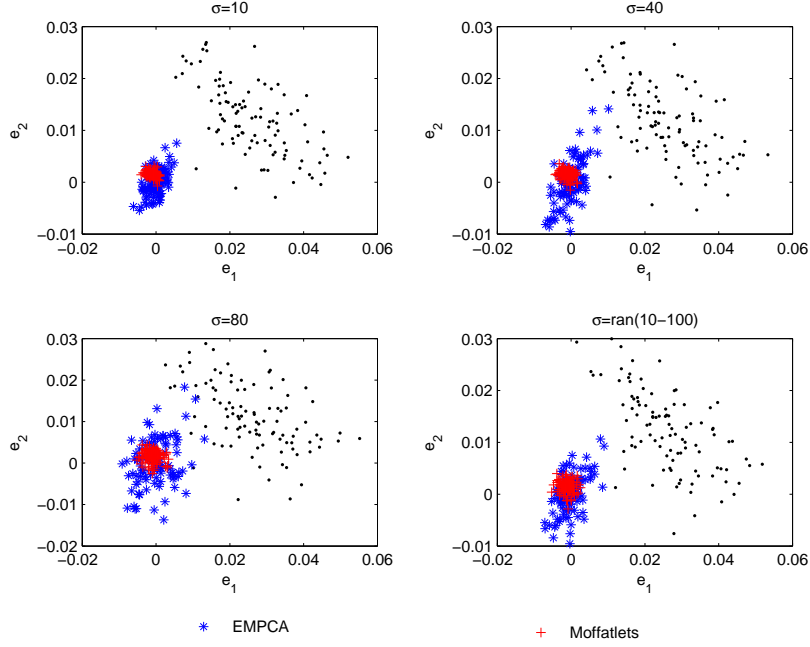


Fig. 14 $(\delta e_1, \delta e_2)$ plotted for the test of data set R02S01-diffraction-OFF. In the figure, there are two kinds of spots: Black spots are ellipticity (e_1, e_2) measured from original stars when background noise are not added yet; Colorful spots (blue and red) are ellipticity difference $(\delta e_1, \delta e_2)$ between the original stars and reconstructed stars using EMPCA and Moffatlets correspondingly. In Fig. 15, 16, 17 we use the same color denotation.

Appendix A: MATHEMATICAL DERIVATION OF RADIAL FUNCTIONS OF MOFFATLETS

In this appendix, we give the derivation of the radial fuctions of the mofattlets, showing that the basis functions have an analytic form. We require the radial basis functions are modified by a weight function with moffat profile

$$Q_l(r) = R_l(r)w(r), w(r) = [1 + (\frac{r}{r_d})^2]^{-\beta}. \quad (\text{A.1})$$

The radial basis functions satisfy

$$2\pi \int_0^{+\infty} dr r R_l(r) R_{l'}(r) e^{-u(r)} = \delta_{ll'}, \quad (\text{A.2})$$

where

$$u(r) = -\ln[1 + (\frac{r}{r_d})^2]^{-2\beta}. \quad (\text{A.3})$$

The corresponding invers function is

$$r = a(u) = r_d \sqrt{e^{u/2\beta} - 1} \quad (\text{A.4})$$

And we have

$$r dr = \frac{r_d^2}{4\beta} e^{\frac{u}{2\beta}} du, \quad (\text{A.5})$$

Then Eq.A.2 reads

$$\frac{\pi r_d^2}{2\beta} \int_0^{+\infty} du R_l[a(u)] R_{l'}[a(u)] e^{-(1-1/2\beta)u} = \delta_{ll'}. \quad (\text{A.6})$$

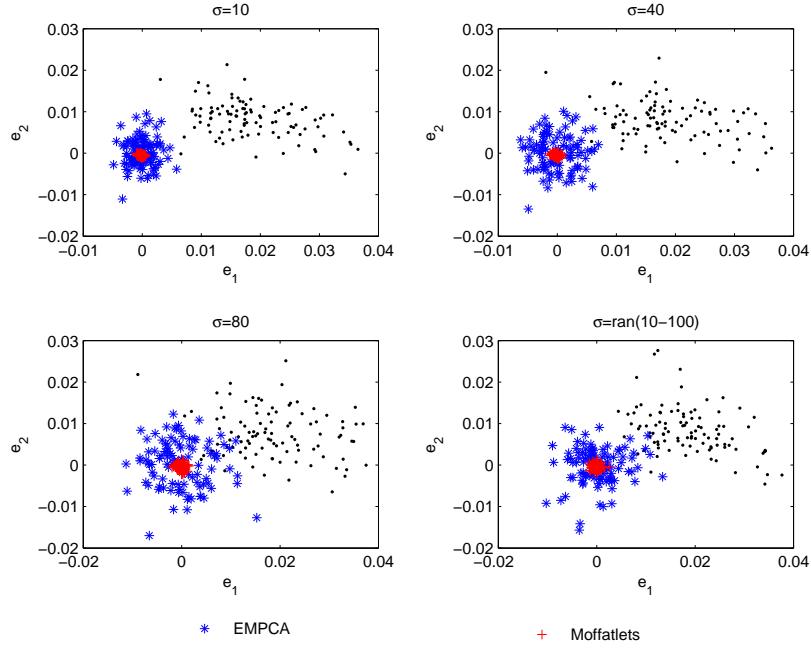


Fig. 15 $(\delta e_1, \delta e_2)$ plotted for the test of data set R02S01-diffraction-ON.

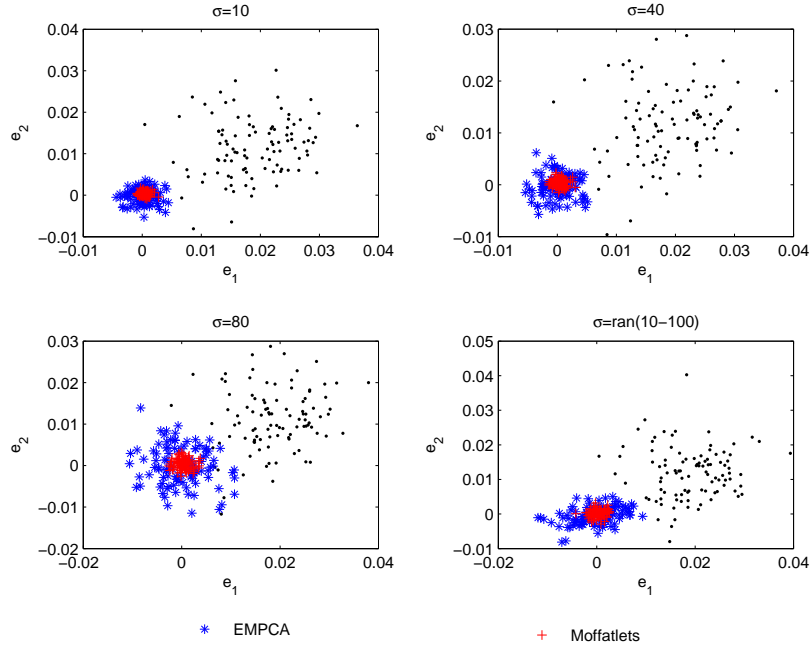


Fig. 16 $(\delta e_1, \delta e_2)$ plotted for the test of data set R22S11-diffraction-OFF.

We change the variables according to $v(u) = (1 - 1/2\beta)u$ and introduce a new function to relate r and v as $r = b(v)$.

Eq.A.2 reads

$$\frac{\pi r_d^2}{2\beta - 1} \int_0^{+\infty} dv R_l[b(v)] R_{l'}[b(v)] e^{-v} = \delta_{ll'}. \quad (\text{A.7})$$

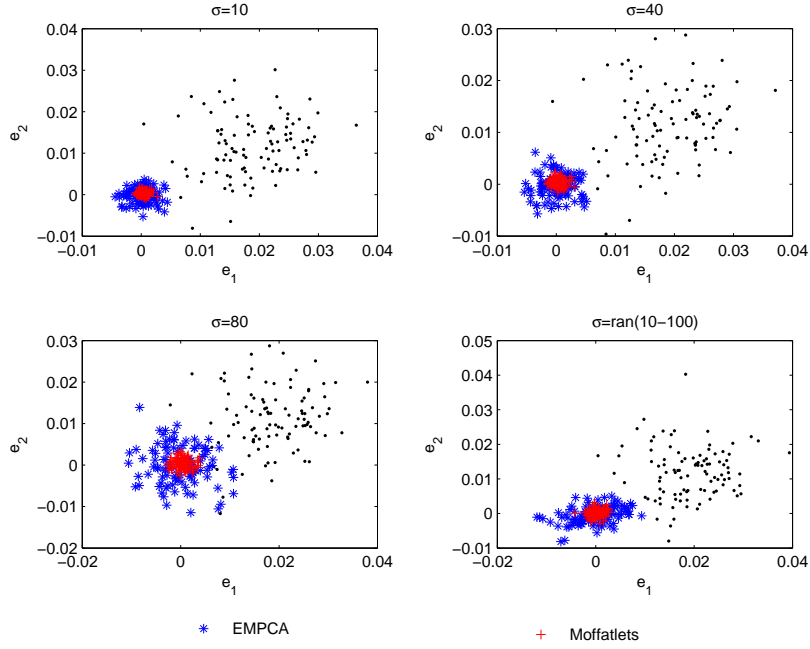


Fig. 17 $(\delta e_1, \delta e_2)$ plotted for the test of data set R22S11-diffraction-ON.

We noticed that this equation is similar with weighted integration of Laguerre ploynomials (Eq.4)

$$\int_0^{+\infty} dv L_l(v) L_{l'}(v) e^{-v} = \delta_{ll'}. \quad (\text{A.8})$$

Then we have

$$R_l(r) = \sqrt{\frac{2\beta-1}{\pi r_d^2}} L_l[v(r)], \quad (\text{A.9})$$

where

$$v(r) = \left(\frac{1}{2\beta} - 1\right) \ln\left[1 + \left(\frac{r}{r_d}\right)^2\right]^{-2\beta}. \quad (\text{A.10})$$

The final radial basis function reads

$$Q_l(r) = \sqrt{\frac{2\beta-1}{\pi r_d^2}} L_l[v(r)] \left[1 + \left(\frac{r}{r_d}\right)^2\right]^{-\beta}. \quad (\text{A.11})$$